Supporting information：

2D Photocatalysts with Tuneable Supports for Enhanced Photocatalytic Water Splitting

Yiyang Li[1], Simson Wu[1], Jianwei Zheng[1], Yung-Kang Peng[1], Dharmalingam Prabhakaran[2], Robert A. Taylor[2] and Shik Chi Edman Tsang[1*]

[1]Wolfson Catalysis Centre, Department of Chemistry, University of Oxford, Oxford, OX1 3QR, UK

[2]Clarendon Laboratory, Department of Physics, University of Oxford, OX1 3PU, UK

*Correspondence to: edman.tsang@chem.ox.ac.uk

This file includes:

Supplementary Methods

Figures S1-S19

Tables S1-S4

Supplementary discussion

References 1-27

Supplementary Methods

Synthesis of CeO_2 nanocubes (NC) and nanospheres (NS)

The synthesis of CeO_2 (100) nanocubes was carried out via hydrothermal process based on previously reported literature [1,2]. 1.0 g of $Ce(NO_3)_3 \cdot 6H_2O$ were added to a 60 mL of 15 M NaOH solution stirred vigorously for 15 min. Afterwards, the solution was transferred to Teflon lined autoclave inside an oven of 180 ^oC for 12 h. Following hydrothermal synthesis, the autoclave was allowed to naturally cool to room temperature. The obtained powder was separated by centrifugation, and then washed 3 times with DI water and dried at 70 ^oC under vacuum overnight.

For the synthesis of CeO_2 nanospheres [3], 1 mmol of $Ce(NO_3)_3 \cdot 6H_2O$ was dissolved in 32 mL of 0.078 M NaOH aqueous solution in a 100 mL round bottom reaction flask. The mixture was stirred at room temperature for 24 h in air, and the colour changed to pale yellow. The CeO_2 nanospheres were collected by centrifugation at 5000 rpm for 10 min, and washed with ethanol and DI water each for three times. Then dried at 70 ^oC under vacuum overnight and collected for further use.

Synthesis of MgO (111), MgO (100)

MgO (111) was prepared by a hydrothermal method. Typically, $MgCl_2 \cdot 6H_2O$ (2 g) and benzoic acid (0.12 g) was dissolved in 60mL deionized water at room temperature. The mixture was stirred for 10 minutes. 2M NaOH (20 mL) was then added drop wise into the solution, forming a white precipitate. The slurry was subsequently transferred to a 100mL autoclave and gradually heated to 180 ^oC and maintained at this temperature for 24 hours. The $Mg(OH)_2$ precursor was obtained after filtration followed by washing with water and drying at 80 ^oC under vacuum overnight. MgO (111) nanosheets were obtained after calcination in compressed air at 500 ^oC for 6 hours [4,5].

MgO (100) was prepared by calcination of magnesium nitrate. In a typical synthesis, $Mg(NO_3)_2$ was placed in a quartz boat in a tubular furnace, and then calcined at 500 ^oC in air flow for 6 hours [6].

Synthesis of ZnO nanoplates and nanorods

The synthesis of ZnO (0001) nanoplates (NPs) was prepared according to our previous report [7,8]. 6.0 g zinc acetate dihydrate ($Zn(Ac)_2 \cdot 2H_2O$) and 3.84g hexamethylenetetramine (HMT, $C_6H_{12}N_4$) were dissolved in 48 mL deionized water. The solution was transferred into a 100 mL Teflon-lined autoclave after a 10-min stirring. The autoclave was then put into an oven and maintained at 100 °C for 24 h and then allowed to cool to room temperature naturally. The white precipitate was collected by centrifugation at 5000 rpm for 10 min, after which the supernatant was decanted and discarded. The solid was washed repeatedly with ethanol and water to remove excess precursor. All ZnO NPs was dried at 70 ^oC overnight and then calcined in air at 450 °C for 2 h with a heating rate of 10 °C/min.

The synthesis of ZnO nanorods (NRs) was also based on our previous report [7,8]. 1.487 g zinc nitrate hexahydrate ($Zn(NO_3)_2 \cdot 6H_2O$) and 6 g NaOH were dissolved in 10 mL deionized water. Then 100 mL ethanol was added to the Zn precursor solution, afterwards 5 mL of 1,2-

ethanediamine (EDA) was also put into the mixture and then the mixture was transferred to a covered plastic container with a volume capacity of 250 mL. The reaction container was kept at room temperature under constant stirring for about 3 days. After the synthesis a white precipitate was centrifuged and washed with DI water and ethanol repeatedly. All ZnO NRs was dried at 70 ^{o}C overnight and then calcined in air at 450 °C for 2 h with a heating rate of 10 °C/min.

Synthesis of layered double hydroxides (LDHs)

All LDHs were synthesized by similar co-precipitation method: Magnesium nitrate ($MgCl_2$) and corresponding trivalent metal precursor ($CrCl_3 \cdot 6H_2O$, $Fe(NO_3)_3 \cdot 9H_2O$, $Co(NO_3)_2 \cdot 6H_2O$ and $Al(NO_3)_3 \cdot 9H_2O$ for MgCr-LDH, MgFe-LDH, MgCo-LDH and MgAl-LDH, respectively) were dissolved in 100 mL Milli-Q water firstly. And then this solution and 1 M NaOH (aq.) were added simultaneously into 25 mL water in a 250 mL three-neck round bottom flask. The pH was maintained at 8-12 depending on the LDH. Afterwards the slurry was kept under vigorous stirring for 2h before centrifugation and washing with water. The obtained solid product was dispersed in water for further use.

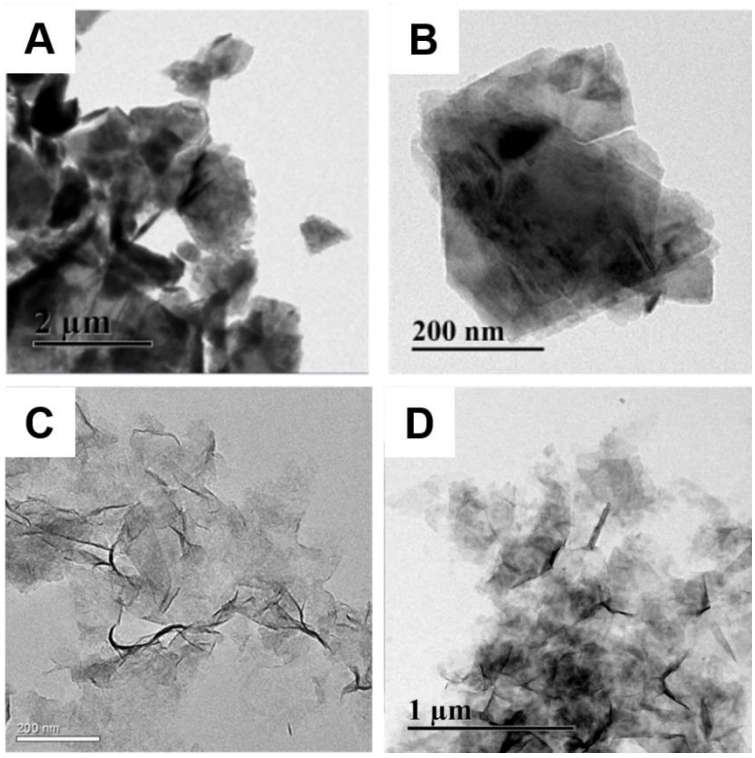

Figure S1. Conventional TEM image analyses of (A, B) bulk MoS_2, showing layered structure of crystal MoS_2, with lateral size varying from 0.5 to 2μm; (C) SL-MoS_2 and (D) Co:SL-MoS_2. After the incorporation of Co atoms, the morphology of SL-MoS_2 remains a sheet-like structure [9].

From the above TEM results, the bulk MoS_2 shows extensive layered structure, with the lateral size of 0.5-2 μm. While after the chemical exfoliation process, the sheet-like MoS_2 monolayers

are successfully obtained, which can be maintained even after the metal doping *via* hydrothermal process. Similar observations for well dispersion are also made from our XRD analysis, which is shown in the Fig. S3. The sharp peaks of bulk MoS_2 almost disappeared after exfoliation, again indicating the successful fabrication of MoS_2 monolayers. Moreover, the commercially available bulk MoS_2 has been extensively studied and presented in literature.

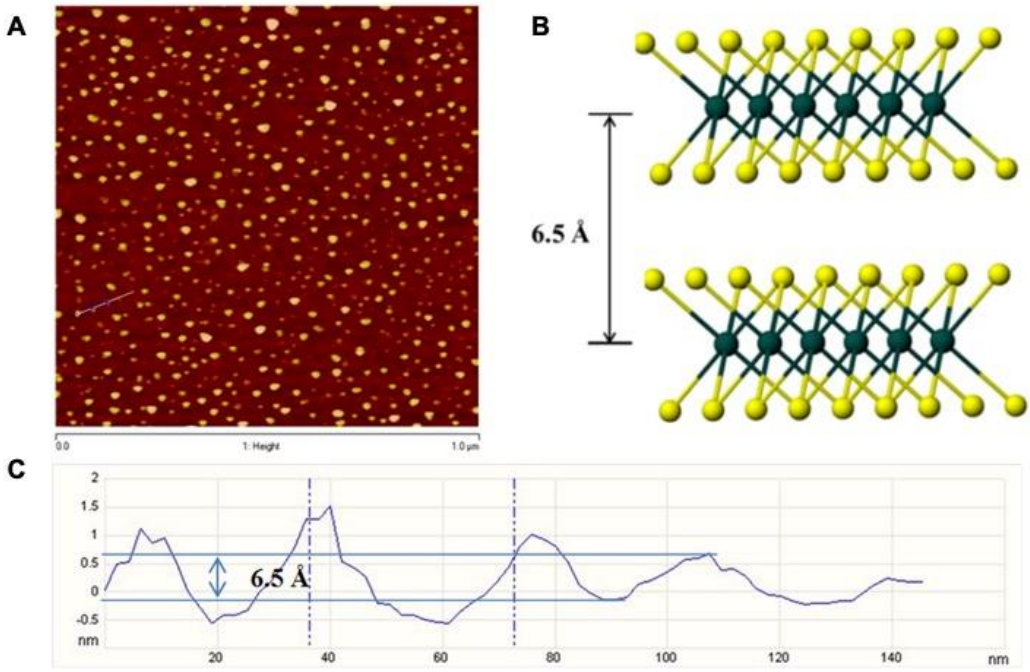

Figure S2. Atomic force microscopy (AFM) image analyses for the fresh chemically exfoliated MoS_2. (A) An AFM image of spin coated SL-MoS_2 on Si substrate surface and (B) a model of 2-H MoS_2 structure perpendicular to c axis, 100 flakes are scanned with majority of heights between 0.6-0.7nm. The lateral dimension of this SL-MoS_2 nanosheet is approximately 20-40 nm. (C) It can be seen that the step heights of individual layers of 0.6-0.7 nm, which is comparable to ca. 0.65 nm of a single layer S-Mo-S building block. Statistical analysis of 100 flakes produced by the lithium exfoliation method revealed that 56% of the flakes to be monolayer, 28% of two layers and 13% of three layers and so on. The average topographic height is around 1.04 nm, which agrees with typical height of a SL-MoS_2 with the presence of water molecules (between 0.6 and 1.0 nm) [9].

It is noted that the dispersion of single molecular layer sample from colloid solution to solid form for characterization is highly dependent on the nature of sample preparation method. The sample characterized by AFM was prepared by spin coating, which allowed the dispersion of thin flakes on the Si substrate surface. And it showed that 56% of the sample to be monolayer, 28% of two layers and 13% of three layers and so on (Figure S2).

However, the TEM sample was prepared by placing a droplet of aqueous SL-MoS_2 colloid on a copper grid followed by fast evaporation, which would have led to some degree of

aggregation. (Figure S1) The images collected by later STEM (Figure S4) on slowly evaporated sample also all showed mostly single layer and sometimes 2- or 3-layers structures. Thus, the aggregation observed in the TEM (Figure S1) was mainly due to the artefact in this sample preparation.

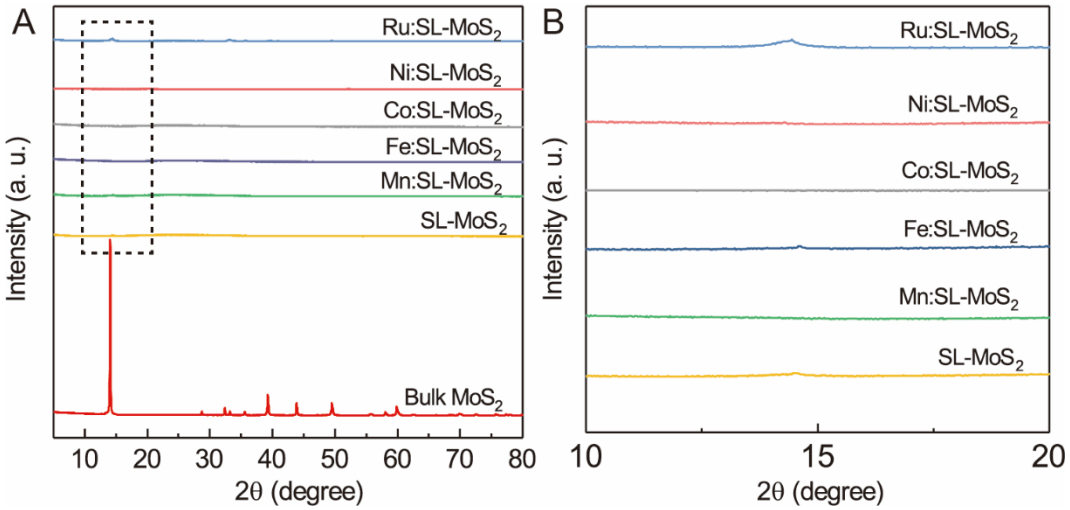

Figure S3. (A) XRD patterns of bulk MoS_2, SL-MoS_2 and the metal-doped SL-MoS_2; (B) Enlarged XRD patterns of SL-MoS_2 and the metal-doped SL-MoS_2 in the range of 10-20^o, as indicated in (A). The above study indicates the stacking peak of MoS_2 at ~15^o is greatly reduced due to the exfoliation of bulk MoS_2. Also, there is no peak seen for metal nanoparticle suggesting the extensive dispersion of the metal precursors.

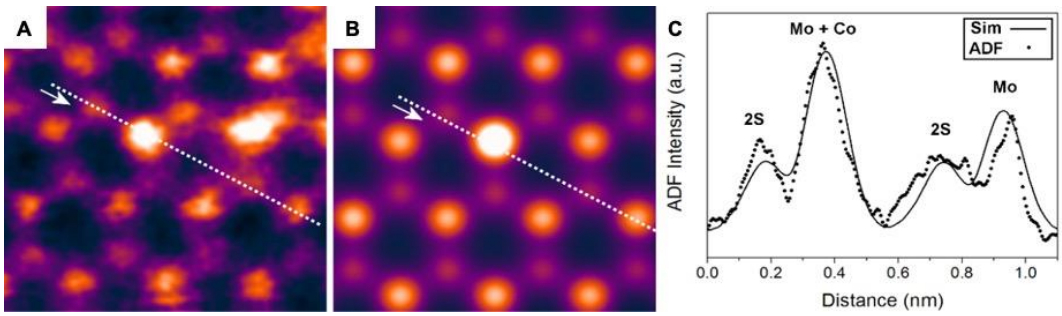

Figure S4. ADF intensity analysis of a Co on Mo top site in monolayer MoS_2.(A) ADF-STEM image of a Co on Mo top site (trigonal site of 3 surface S atop to Mo as the most probable site), as in the main text. (B) Image simulation of the Co on Mo top site, using DFT optimized geometry for the atomic coordinates. (C) ADF intensity profiles of the experimental (scatter) and simulation (line) taken from the annotated lines in (A) and (B), showing good agreement [9].

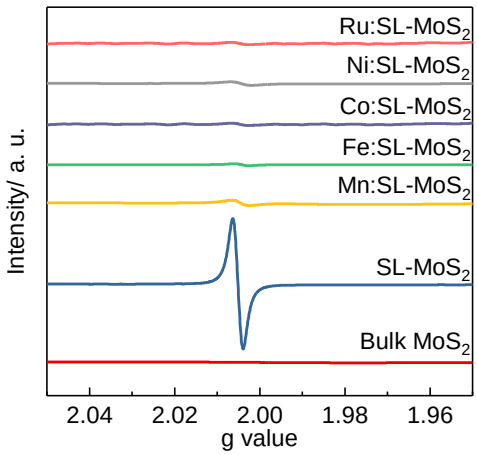

Figure S5. EPR spectra of bulk MoS_2, SL-MoS_2 and the metal-doped SL-MoS_2.

It is noted that the EPR signal disappearance of SL-MoS_2 upon adding metals can be due to two possibilities, namely: metal atom occupies to S vacant site or progressive metal cluster formation. The STEM image of the Ru:SL-MoS_2 sample shown in Fig. 1E in the main manuscript as well as Co-doped SL-MoS_2 demonstrate that the metal atoms introduced by the hydrothermal process can occupy atop site to Mo (most probable site) and the S-vacant site [9]. In addition, according to our TEM and STEM images, there was no sign of extensive clusters formation under our given loading. The corresponding XRD after the metal doping process gives no indication for bulk MoS_2 reformation nor metal nanoparticle aggregation. Moreover, XANES and EXAFS carried out for Ru:SL-MoS_2, as shown in Fig. 1F and 1G indicate that the Ru oxidation state remains zero with no Ru-Ru bond. Instead, the Ru-S scattering observed in the EXAFS gives a coordination number of 2.8 indicating that the Ru atoms are anchored in the S-vacancy sites as well as atop site to Mo by 3 nearest S atoms [9]. Thus, experimental evidence suggests that single atom dwells on the S site to account for the EPR signal disappearance. However, we cannot rule out there is a small degree of metal clustering formation.

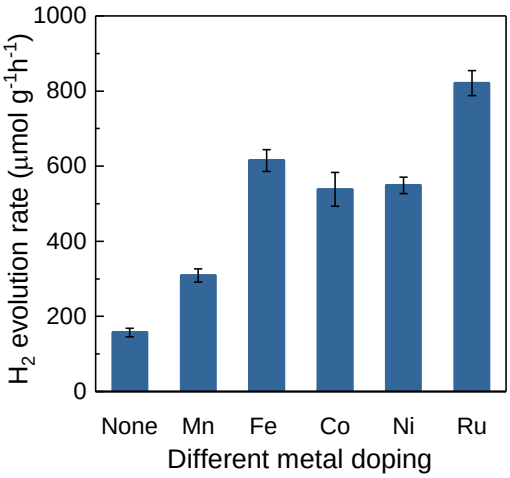

Figure S6. Photocatalytic water splitting performance over different metal-doped MoS_2 single layer per gram basis. Overall water splitting reaction was carried out at 270 ^oC in Ar with a fixed amount of water in an autoclave: H_2 and O_2 products were quantified by a GC equipped with TCD detector.

As is well known, hydrogen evolution reaction (HER) plays a significant role in water electrolysis, for which precious group metals such as Pt and Ru commonly display highest activity [10–12]. It is also consented that the HER efficiency is related to the strength of the metal-hydrogen bonding on the surface of the catalysts and the overpotential required for hydrogen reduction[10]. The adsorption energy for metal-H should be neither too high nor too low for efficient HER. Typically, Ru is closer to the centre with optimum H adsorption energy [11], hence can give low overpotential for hydrogen reduction [10,12]. As seen from Fig. S6 that a similar volcano activity curve in our photo water splitting was peaked at Fe in the first-row transition metals with electronic modification from the MoS_2 from our experiment. Indeed, the use of precious metal Ru (moving one element down the group of Fe) can further enhance the M-H interaction, giving higher activity for water splitting. We therefore believe that our observation of the superior activity of Ru-doped SL-MoS_2 is consistent with the previous studies in H_2O activation for H_2 production in literature.

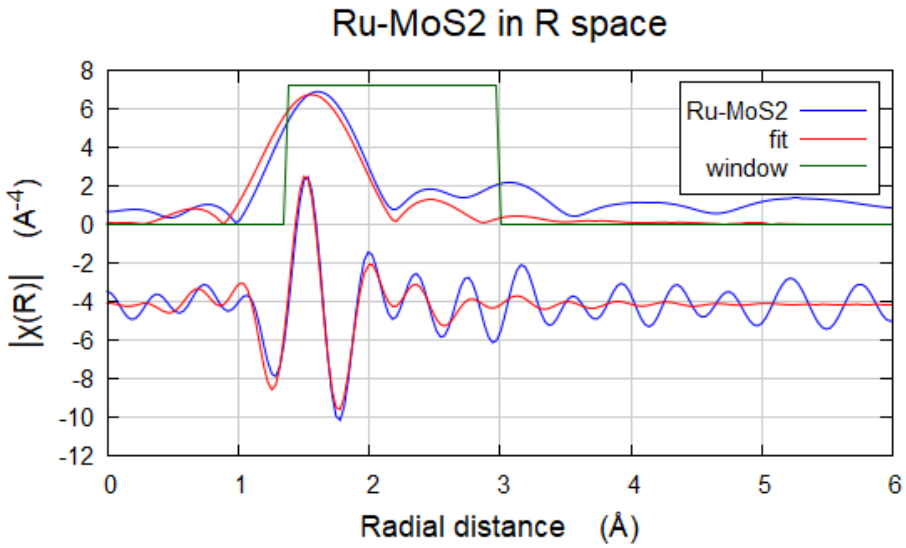

R-factor: 3.5%

Scattering path	Bond distance (Å)	Coordination Number	Debye Waller's factor
Ru-S	1.98 +/- 0.03	2.8 +/- 0.3	0.007

Figure S7. ex-situ EXAFS fittings of the Ru:SL-MoS_2. Quantitative details derived from the fitting are shown in the table.

Polar and Non-polar oxides

For low-index surfaces of metal oxides. The oxygen ion terminated facets are well-known to have a significant net dipole moment perpendicular to its surface, thus regarded as a polar surface. Any variation in the surface properties of the different surfaces would lead to a difference in their metal-support interaction(s) and the modification of the unique properties of oxide support mentioned earlier. According to the Wulff construction, the crystal planes exposed on the surface of a crystalline material are determined by its morphology. Thus, the surface exposed by a nanoparticle can be influenced by controlling its morphology and this has led to desire for the morphology-controlled synthesis of various materials. It has been reported that CeO_2, CuO, TiO_2 and Co_3O_4, show examples of different morphologies such as nano-sized cubes, rods, belts, plates and octahedrons [8]. Varying the exposed surface facets exposed of the oxide support nanoparticle will result in an alteration of its surface chemistry, which in turn will influence its catalytic properties. It has been argued that it is possible to produce a net dipole moment perpendicular to the surface with alternately charged planes with a repeat unit consisting of only two planes. As a result, for example, polar CeO_2 (100) surface is highly unstable due to the strong electrostatic repulsion of similar charged ions within the same plane. There are a number of ways for a polar surface to reduce its high surface energy, namely bringing in opposite charged species on its polar surface from the environment through an adsorption process. Alternatively, surface reconstruction by removing oxygen to generate oxygen vacancies and simultaneously altering the oxidation state of metal cations, favourable for transition metal oxides, will reduce or eliminate surface polarity. The latter is expected to take place in the case of CeO_2 where redox process involving the cerium ions can occur with low activation energy. This accounts for the higher quantity of oxygen vacancies we observed over our Ce (100) samples by Electron Paramagnetic Resonance (EPR).

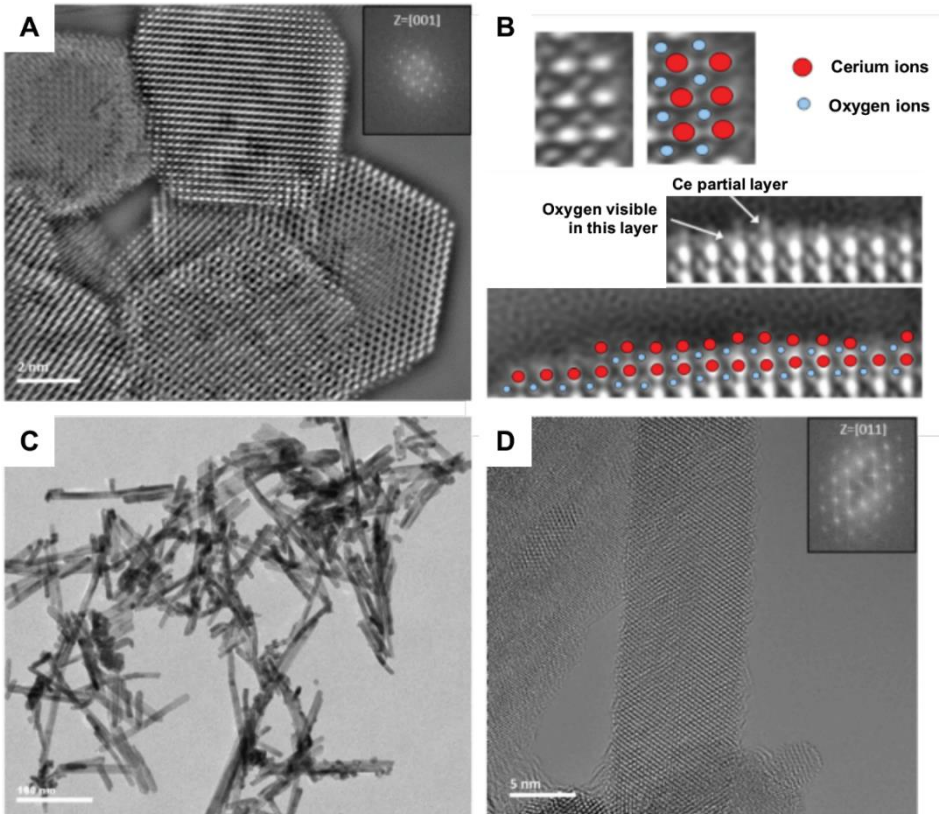

Figure S8. (A) Exit wave restoration image of polar-faceted CeO_2 nanocubes with predominant polar (100) surfaces where deviations to hexagonal shape with reconstructed (111) facets can be seen; (B) High magnification of the exit wave restoration showing the (100) showing discrete alternative atomic layers of Ce^{3+}/Ce^{4+} and O^{2-} ions can be visualized and indexed matching with corresponding (100) model; (C) TEM image of CeO_2 nanorods; (D) predominant non-polar (110) surface with inter-dispersed Ce cations and O anions but also containing small degrees of other reconstructed surfaces of (111) and (100) surfaces [13].

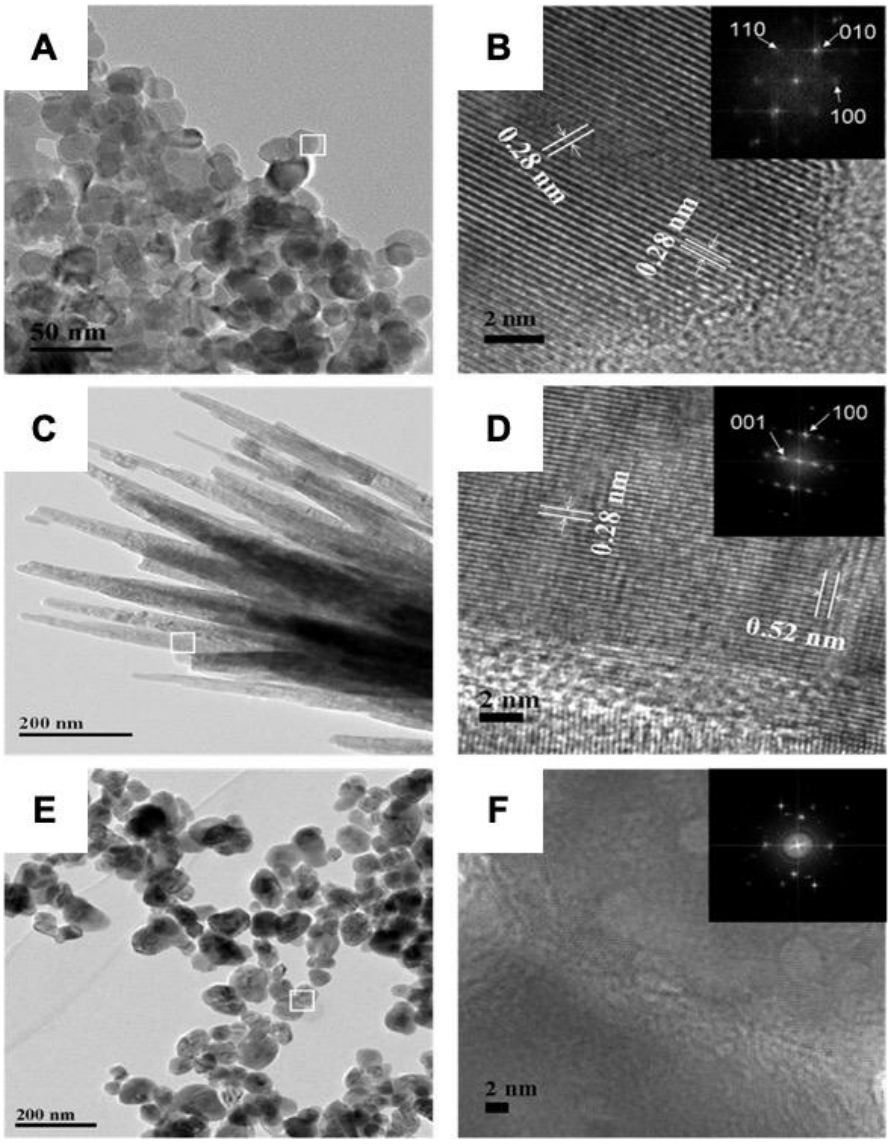

Figure S9. TEM and HRTEM images of ZnO (A, B) polar-faceted nanoplates; (C, D) non-polar nanorods and (E, F) polycrystalline powder. Inset: corresponding electron diffraction (ED) pattern of ZnO nanoplates, nanorods and powder [8].

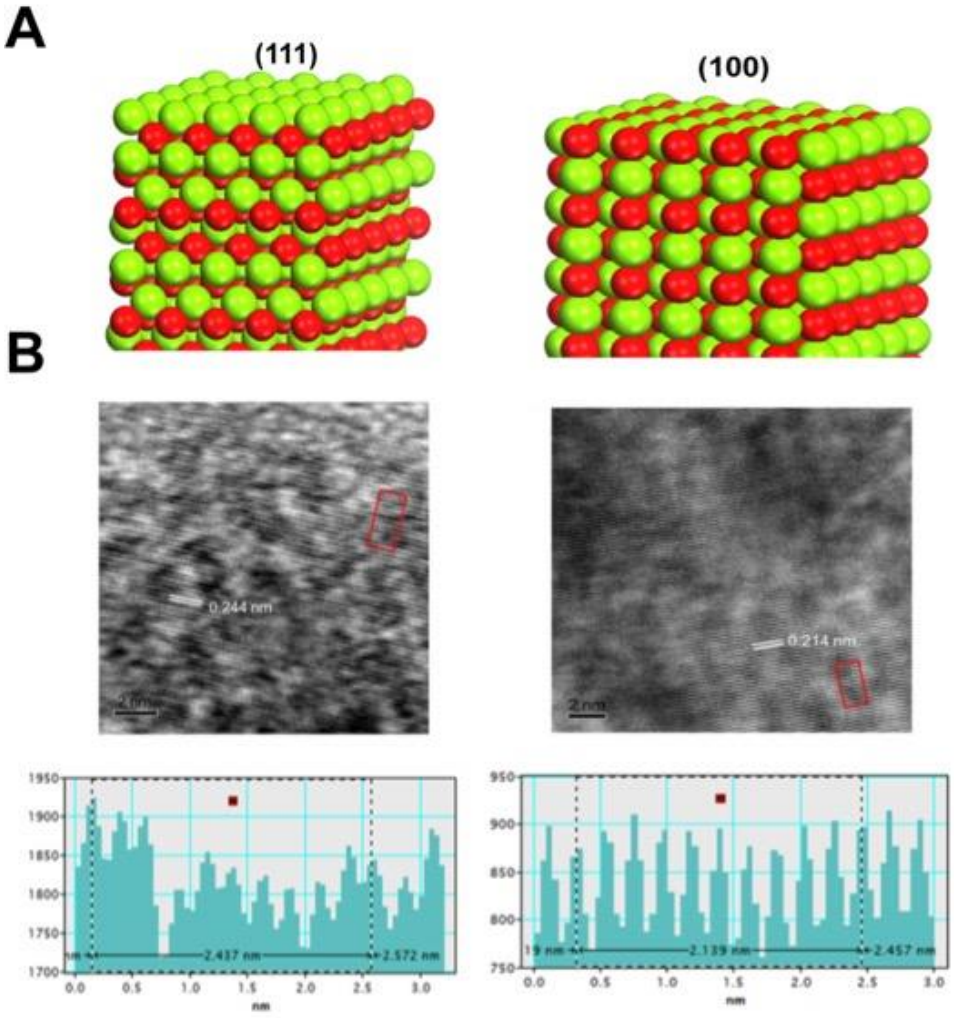

Figure S10. (A) Schematic illustrations of micro-size MgO facets: polar Mg-terminated (111), non-polar MgO (100) (O: red; Mg: green), (B) TEM and HRTEM of MgO (111) and (100), the measured lattice fringes are consistent with the lattice parameters.

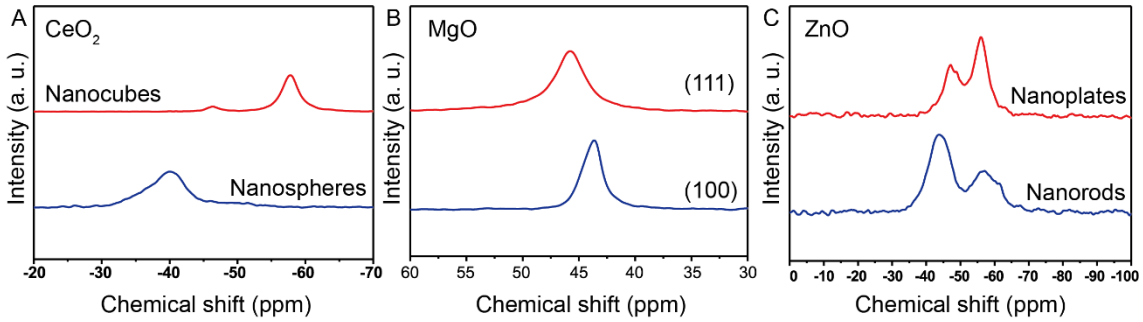

Figure S11. (A) TMP-probed ^{31}P NMR of polar CeO_2 nanocubes and non-polar nanospheres; (B) TMPO-probed ^{31}P NMR of polar MgO(111) and non-polar MgO(100); (C) TMP-probed ^{31}P NMR of polar ZnO nanoplates and non-polar nanorods. As seen clearly, the surface polarity of the polar faceted oxides such as CeO_2(100) and ZnO (0001) show higher shielding of the TMP probe molecules and lower de-shielding of polar MgO (111) sample.

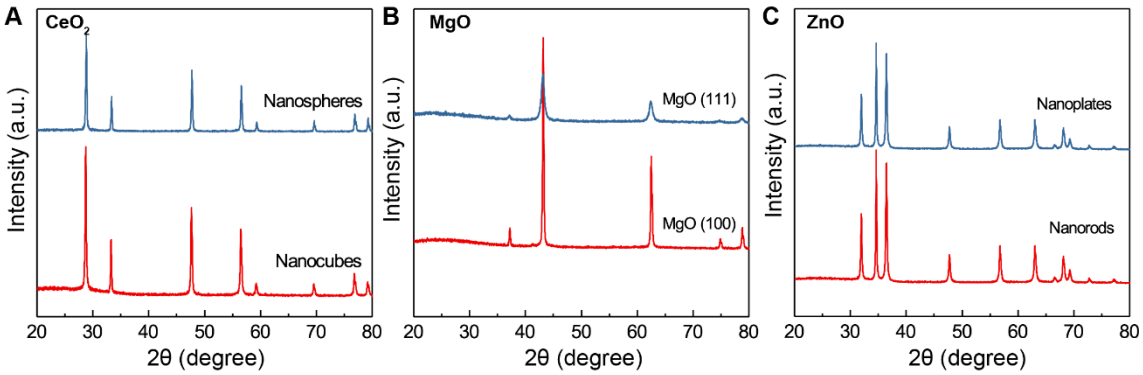

Figure S12. XRD patterns of polar and non-polar faceted (A) CeO_2, (B) MgO and (C) ZnO. Due to the random orientation of each nanoparticles the similarity in the XRD patterns for both polar and non-polar faceted particles suggest that XRD cannot be used to differentiate them.

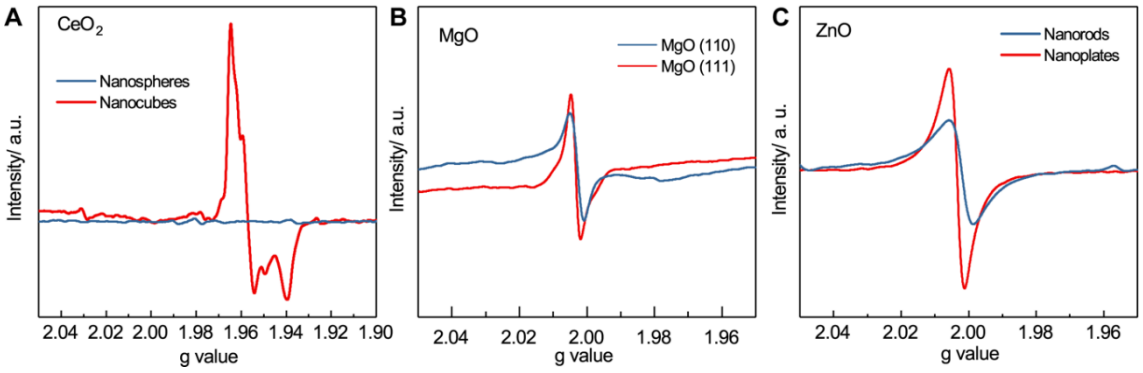

Figure S13. EPR spectra of polar and non-polar faceted (A) CeO_2, (B) MgO and (C**)** ZnO. The polar oxides CeO_2 NCs, MgO (111) and ZnO (0001) nanoplates give higher degree of oxygen vacancies (higher EPR signals due to O_2 on the vacancy to form O_2^-)

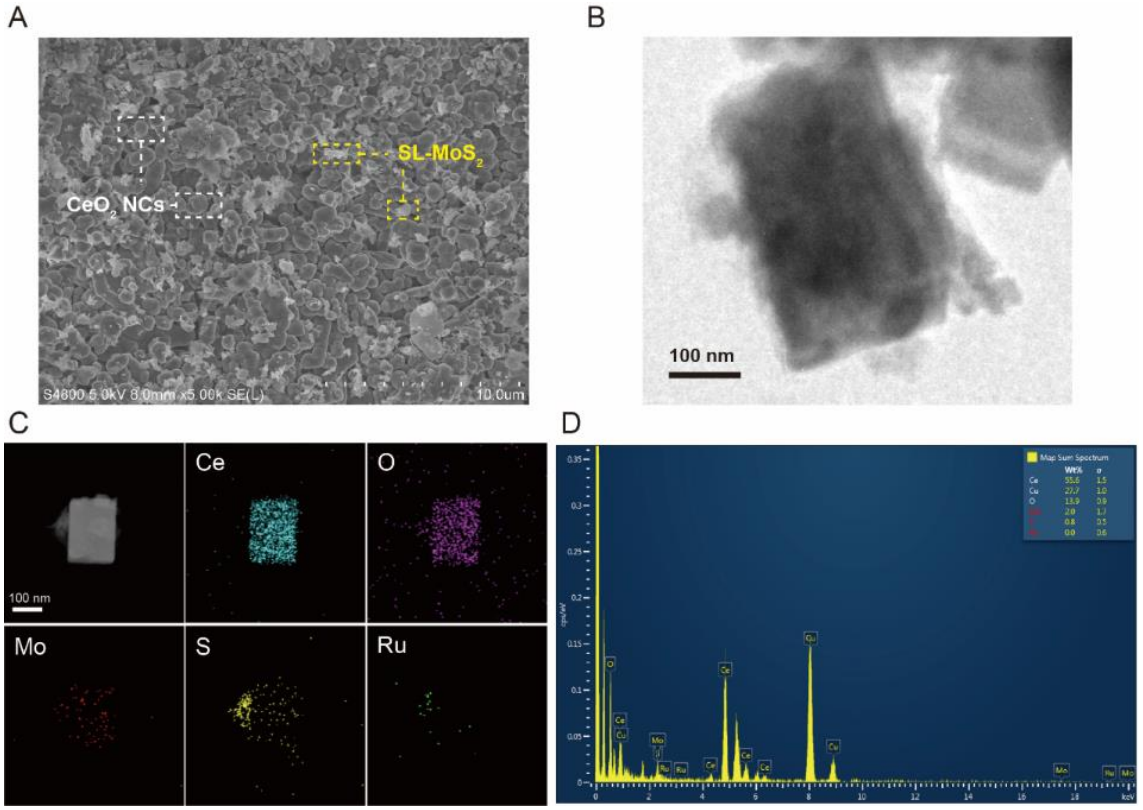

Figure S14. (A) SEM images of Ru:SL-MoS_2/CeO_2 NCs; (B, C) TEM and EDS elemental mapping of selected Ru:SL-MoS_2 on a cubic CeO_2 particle; (D) EDS spectrum of (B, C).

The imaging of the physical mixture is challenging in obtaining high resolution of the interfacial materials due to the dominant quantity and feature of supports in our mixed ratios. As seen from the typical SEM and TEM on the Ru:SL-MoS_2 on polar CeO_2 nanocubes in Fig.

S14, SL-MoS_2 (layers) appears to disperse on CeO_2 particles well over the large area. This suggests the extended interface can give desirable active phase-support interactions as described in this paper. There seems to be some degree of restacking of the overlying MoS_2 layers, however, XRD indicated no major restacking, see Fig. S3. So further optimisation in the interfacial dispersion may also be required.

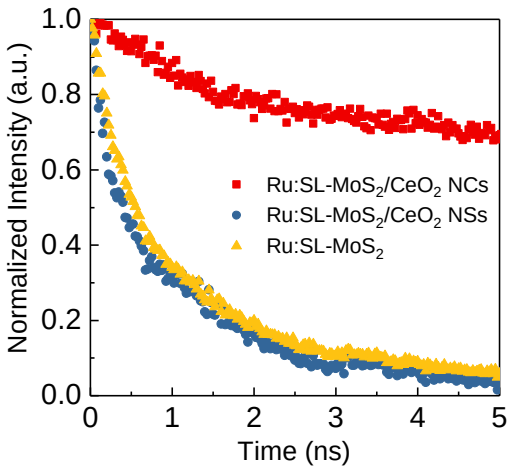

Figure S15. TRPL spectra of Ru:SL-MoS_2, Ru:SL-MoS_2/CeO_2 NCs (Nanocubes) and Ru:SL-MoS_2/CeO_2 NSs (Nanospheres)**.**

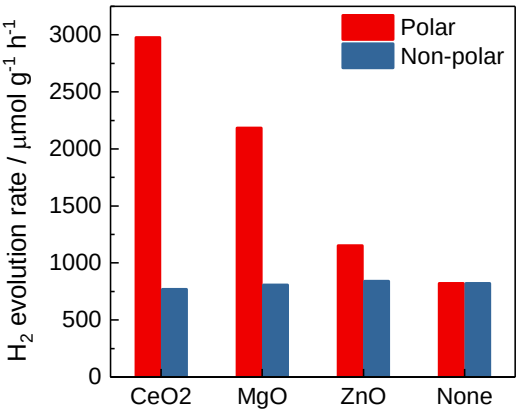

Figure S16. Comparison of the photocatalytic activities of the Ru:SL-MoS_2 combined with polar faceted oxide supports: CeO_2 NCs, MgO (111) and ZnO NPs and their non-polar counterparts at 270^{o}C in water-catalyst mixture in an autoclave.

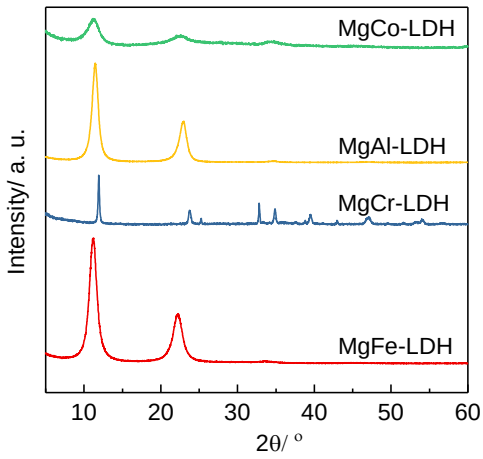

Figure S17. XRD patterns of different Mg-contained LDHs prepared by co-precipitation method.

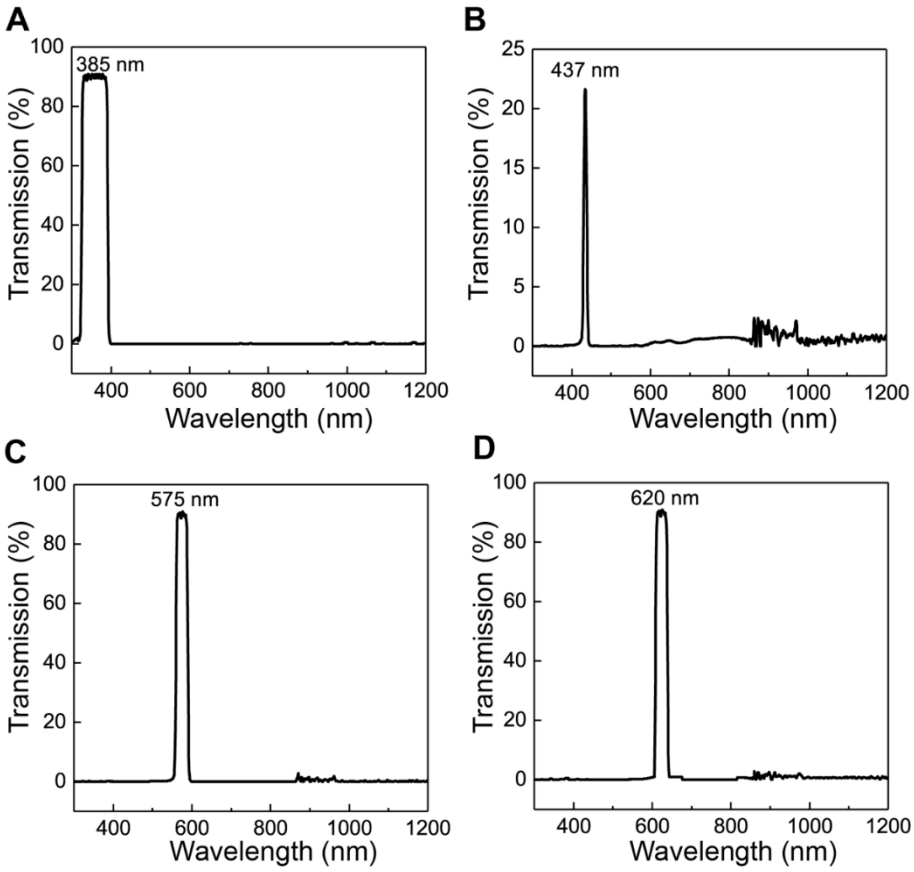

Figure S18. UV-Vis transmission bandpass filters which were used in Q.E. measurements.

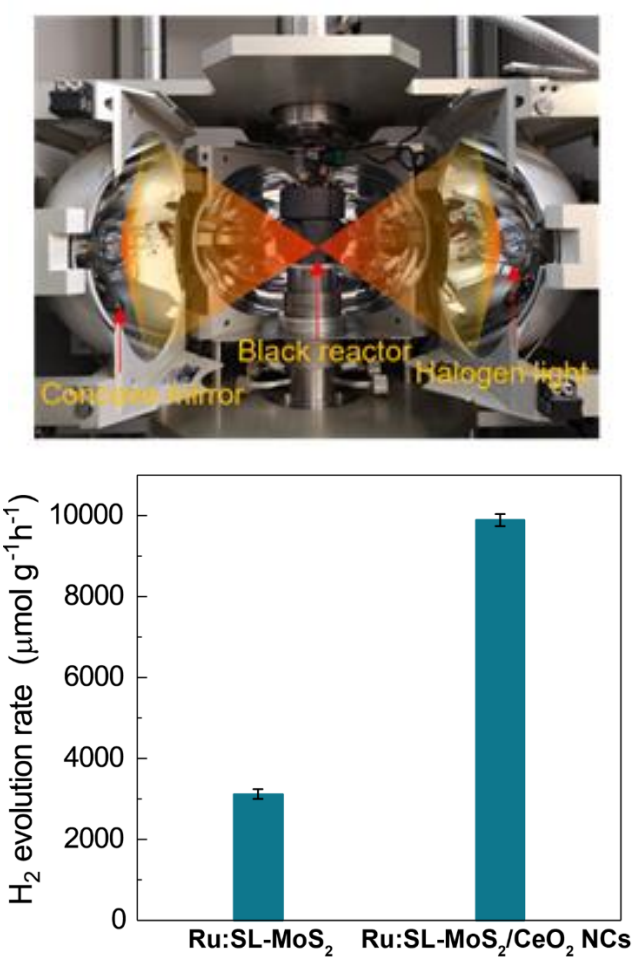

Figure S19. A photographic image of a four-mirror floating-zone solar furnace from Crystal Systems Inc. (top image) used to mimic a solar concentrator to focus a light beam to provide both heat and photons to the catalysts without any other energy input from an electrical device. Photocatalytic water splitting activities per gram of catalyst (bottom image) at 270 ℃ in an autoclave obtained from light furnace with concentrated light illumination over Ru:SL-MoS_2 with and without polar CeO_2 NCs, the analysis errors are also given.

Table S1. Photocatalytic activities of MoS_2 based materials.

Entry	Photocatalysts[1]	H_2 evolution rate/ μmol h^{-1} g^{-1}
1	Bulk MoS_2	N. A.
2	SL-MoS_2	157±11
3	Ru:SL-MoS_2	821±33
4	Mn:SL-MoS_2	309±18
5	Fe:SL-MoS_2	615±29
6	Co:SL-MoS_2	538±45
7	Ni:SL-MoS_2	549±22
8	Ru:SL-MoS_2/CeO_2 NCs	2977±85
9	Ru:SL-MoS_2/CeO_2 NSs	770±31
10	Ru:SL-MoS_2/MgO (111)	2184±76
11	Ru:SL-MoS_2/MgO (100)	808±40
12	Ru:SL-MoS_2/ZnO NPs	1152±65
13	Ru:SL-MoS_2/ZnO NRs	839±29
14	Ru:SL-MoS_2/MgAl-LDH	1811±60
15	Ru:SL-MoS_2/MgCo-LDH	1431±43
16	Ru:SL-MoS_2/MgCr-LDH	1670±53
17	Ru:SL-MoS_2/MgFe-LDH	1520±59
18	CeO_2 NCs	N. A.
19	CeO_2 NSs	N. A.
20	MgO (111)	N. A.
21	MgO (100)	N. A.
22	ZnO NPs	N. A.
23	ZnO NRs	N. A.
24	MgAl-LDH	N. A.
25	MgCo-LDH	N. A.
26	MgCr-LDH	N. A.
27	MgFe-LDH	N. A.

[1] 2 mg of SL-MoS_2 was used in each photocatalytic activity test for Entry 1-7 (4 mg catalyst in all was used for the 50:50 wt.% mixtures, Entry 8-17), and for Entry 18-27, 5 mg of materials was used. Overall water splitting reaction was carried out at 270 °C in Ar and the products H_2/O_2 was then detected by GC equipped with TCD. The calculation of the activity is based on the amount of the SL-MoS_2 contained in the photocatalysts.

Table S2. Exciton lifetime values and corresponding exponential fitting error of each photocatalyst derived from the time-resolved photoluminescence results in this work.

Entry	Photocatalyst and conditions	Exciton lifetime/ns
1	Ru:SL-MoS_2	1.02±0.01
2	Ru:SL-MoS_2/CeO_2 NCs	4.53±0.05
3	Ru:SL-MoS_2/CeO_2 NSs	1.04±0.03
4	Ru:SL-MoS_2/MgO (111)	3.10 ±0.02
5	Ru:SL-MoS_2/MgO (100)	1.02±0.04
6	Ru:SL-MoS_2/ZnO NPs	1.32±0.03
7	Ru:SL-MoS_2/ZnO NRs	1.03±0.02
8	Ru:SL-MoS_2/MgAl-LDH	2.62±0.05
9	Ru:SL-MoS_2/MgCo-LDH	1.93±0.03
10	Ru:SL-MoS_2/MgCr-LDH	2.32±0.04
11	Ru:SL-MoS_2/MgFe-LDH	2.05±0.02

The exciton lifetime is obtained by fitting corresponding background-corrected PL spectrum with a mono-exponential decay function in the form $y = A_1\exp(-x/t_1) + y_0$. Error in the fitting is determined from its least square.

Table S3. Photocatalytic activity of water splitting in this work at 270° compared to selected literature.

Photocatalyst	Light source and wavelength	H_2 evolution rate /μmol h^{-1} g^{-1}	Ref.
Ru:SL-MoS_2	70 W Tungsten lamp, ≥400 nm	821	This work
Ru:SL-MoS_2/CeO_2 NCs	70 W Tungsten lamp, ≥400 nm	2977	This work
CDots-C_3N_4	300 W Xe lamp, ≥420 nm	566	[14]
Pt/(Cring)-C_3N_4	300 W Xe lamp, ≥420 nm	150	[15]
Pt, Co modified g-C_3N_4	300 W Xe lamp, ≥420 nm	1.2	[16]
Cr-Rh oxide/$(Ga_{1-x}Zn_x)(N_{1-x}O_x)$	450 W high pressure mercury lamp, ≥436 nm	1543	[17]
Ni@NiO_x/$SrTiO_3$	AM 1.5 solar simulator	18	[18]
Pt, Co_3O_4/carbon nitride	300 W Xe lamp, ≥300 nm	155	[19]
Pt/$Bi_xY_{1-x}VO_4$	300 W Xe lamp, ≥300 nm	139	[20]
Co-P/Black phosphorus nanosheet	300 W Xe lamp, ≥420 nm	3290	[21]

Table S4. Quantum efficiency (Q. E.) for water splitting in this work as compared to the selected literature.

Photocatalyst	Co-catalyst	Wavelength/nm	Q. E.*/ %	Ref.
Ru:SL-MoS_2	/	437	16.3	This work
Ru:SL-MoS_2/CeO_2 NCs	/	437	66.8	This work
Black phosphorus nanosheet	Co-P	430	42.55	[21]
Vacuum-activated P25	Pt	420	1.17	[22]
Hydrogenated TiO_2	Pt	420	2.28	[23]
Unsupported Au NPs	/	300	2.7	[24]
W-doped TiO_2	Au	380	18.3	[25]
Hydrogenated N doped-TiO_2	Pt	420	9.0	[26]
Li-EDA treated P25	/	420	2.57	[27]

* Quantum efficiency results from literature were obtained in the presence of various amounts of sacrificial reagent such as methanol, while in this work it was measured in pure water (Milli. Q.).

Supplementary discussion

Calculation of QE.

A typical QE calculation is shown below, taking Ru:SL-MoS_2/CeO_2 NCs as an example:

The hydrogen amount analysed by GC is **3.95 μmol,** corresponding to **2.379×10^{18}** hydrogen molecules;

During a period of 2 hours, the energy of the light irradiation: W= P×t

With the bandpass filter of 437 nm, the light irradiation power is measured to be **P=0.45 mW,** therefore, the energy W=0.00045×7200=**3.24 J,** which contains the photon (437 nm) numbers of **7.123×10^{18}.**

QE (%) = ($2\times3.215\times10^{18}$)/ ($7.123\times10^{18}$) =66.8%

References

[1] L. Torrente-Murciano, A. Gilbank, B. Puertolas, T. Garcia, B. Solsona, D. Chadwick, Appl. Catal. B Environ. 132–133 (2013) 116–122.

[2] H.X. Mai, L.D. Sun, Y.W. Zhang, R. Si, W. Feng, H.P. Zhang, H.C. Liu, C.H. Yan, J. Phys. Chem. B 109 (2005) 24380–24385.

[3] M.J. Manto, P. Xie, C. Wang, ACS Catal. 7 (2017) 1931–1938.

[4] K. Zhu, J. Hu, C. Kübel, R. Richards, Angew. Chem. Int. Ed. 45 (2006) 7277–7281.

[5] J. Hu, K. Zhu, L. Chen, C. Kübel, R. Richards, J. Phys. Chem. C 111 (2007) 12038–12044.

[6] J. Chen, S. Tian, J. Lu, Y. Xiong, Appl. Catal. A Gen. 506 (2015) 118–125.

[7] F. Liao, Y. Huang, J. Ge, W. Zheng, K. Tedsree, P. Collier, X. Hong, S.C. Tsang, Angew. Chem. Int. Ed. 50 (2011) 2162–2165.

[8] Y.K. Peng, L. Ye, J. Qu, L. Zhang, Y. Fu, I.F. Teixeira, I.J. McPherson, H. He, S.C.E. Tsang, J. Am. Chem. Soc. 138 (2016) 2225–2234.

[9] G. Liu, A.W. Robertson, M.M.J. Li, W.C.H. Kuo, M.T. Darby, M.H. Muhieddine, Y.C. Lin, K. Suenaga, M. Stamatakis, J.H. Warner, S.C.E. Tsang, Nat. Chem. 9 (2017) 810–816.

[10] D.H. Kweon, M.S. Okyay, S.J. Kim, J.P. Jeon, H.J. Noh, N. Park, J. Mahmood, J.B. Baek, Nat. Commun. 11 (2020) 1278.

[11] J.R. McKone, E.L. Warren, M.J. Bierman, S.W. Boettcher, B.S. Brunschwig, N.S. Lewis, H.B. Gray, Energy Environ. Sci. 4 (2011) 3573–3583.

[12] J. Mahmood, F. Li, S.M. Jung, M.S. Okyay, I. Ahmad, S.J. Kim, N. Park, H.Y. Jeong, J.B. Baek, Nat. Nanotechnol. 12 (2017) 441–446.

[13] L. Ye, A.H. Mahadi, C. Saengruengrit, J. Qu, F. Xu, S.M. Fairclough, N. Young, P.L. Ho, J. Shan, L. Nguyen, F.F. Tao, K. Tedsree, S.C.E. Tsang, ACS Catal. 9 (2019) 5171–5177.

[14] J. Liu, Y. Liu, N. Liu, Y. Han, X. Zhang, H. Huang, Y. Lifshitz, S.T. Lee, J. Zhong, Z. Kang, Science 347 (2015) 970–974.

[15] W. Che, W. Cheng, T. Yao, F. Tang, W. Liu, H. Su, Y. Huang, Q. Liu, J. Liu, F. Hu, Z. Pan, Z. Sun, S. Wei, J. Am. Chem. Soc. 139 (2017) 3021–3026.
[16] G. Zhang, Z.A. Lan, L. Lin, S. Lin, X. Wang, Chem. Sci. 7 (2016) 3062–3066.
[17] K. Maeda, K. Teramura, D. Lu, T. Takata, N. Saito, Y. Inoue, K. Domen, Nature 440 (2006) 295.
[18] K. Han, T. Kreuger, B. Mei, G. Mul, ACS Catal. 7 (2017) 1610–1614.
[19] D. Zheng, X.N. Cao, X. Wang, Angew. Chem. Int. Ed. 55 (2016) 11512–11516.
[20] W. Fang, J. Liu, D. Yang, Z. Wei, Z. Jiang, W. Shangguan, ACS Sustain. Chem. Eng. 5 (2017) 6578–6584.
[21] B. Tian, B. Tian, B. Smith, M.C. Scott, R. Hua, Q. Lei, Y. Tian, Nat. Commun. 9 (2018) 1397.
[22] M. Xing, J. Zhang, F. Chen, B. Tian, Chem. Commun. 47 (2011) 4947–4949.
[23] F. Zuo, K. Bozhilov, R.J. Dillon, L. Wang, P. Smith, X. Zhao, C. Bardeen, P. Feng, Angew. Chem. Int. Ed. 51 (2012) 6223–6226.
[24] B. Tian, Q. Lei, W. Zhang, Y. Cui, Y. Tian, B. Tian, Chem. Commun. 54 (2018) 1845–1848.
[25] B. Liu, S. Su, W. Zhou, Y. Wang, D. Wei, L. Yao, Y. Ni, M. Cao, C. Hu, CrystEngComm 19 (2017) 675–683.
[26] K. Zhang, W. Zhou, L. Chi, X. Zhang, W. Hu, B. Jiang, K. Pan, G. Tian, Z. Jiang, ChemSusChem 9 (2016) 2841–2848.
[27] K. Zhang, L. Wang, J.K. Kim, M. Ma, G. Veerappan, C.L. Lee, K.J. Kong, H. Lee, J.H. Park, Energy Environ. Sci. 9 (2016) 499–503.